The Astrophysical Journal Letters, 951:L45 (8pp), 2023 July 10 https://doi.org/10.3847/2041-8213/ace2c9

Evidence for a Black Hole Spin–Orbit Misalignment in the X-Ray Binary Cyg X-1

Andrzej A. Zdziarski[1], Alexandra Veledina[2,3], Michał Szanecki[4], David A. Green[5], Joe S. Bright[6], and David R. A. Williams[7]
[1] Nicolaus Copernicus Astronomical Center, Polish Academy of Sciences, Bartycka 18, PL-00-716 Warszawa, Poland; aaz@camk.edu.pl
[2] Department of Physics and Astronomy, FI-20014 University of Turku, Finland
[3] Nordita, KTH Royal Institute of Technology and Stockholm University, Hannes Alfvéns väg 12, SE-10691 Stockholm, Sweden
[4] Faculty of Physics and Applied Informatics, Łódź University, Pomorska 149/153, PL-90-236 Łódź, Poland
[5] Cavendish Laboratory, 19 J.J. Thomson Avenue, Cambridge CB3 0HE, UK
[6] Astrophysics, Department of Physics, University of Oxford, Keble Road, Oxford OX1 3RH, UK
[7] Jodrell Bank Centre for Astrophysics, School of Physics and Astronomy, The University of Manchester, Manchester M13 9PL, UK
Received 2023 June 2; revised 2023 June 26; accepted 2023 June 29; published 2023 July 13

Abstract

Recently, the accretion geometry of the black hole X-ray binary Cyg X-1 was probed with the X-ray polarization. The position angle of the X-ray-emitting flow was found to be aligned with the position angle of the radio jet in the plane of the sky. At the same time, the observed high polarization degree could be obtained only for a high inclination of the X-ray-emitting flow, indicating a misalignment between the binary axis and the black hole spin. The jet, in turn, is believed to be directed by the spin axis; hence, a similar misalignment is expected between the jet and binary axes. We test this hypothesis using very long (up to about 26 yr) multiband radio observations. We find a misalignment of 20°–30°. However, contrary to the earlier expectations, the jet and binary viewing angles are found to be similar, while the misalignment is seen between the position angles of the jet and the binary axis on the plane of the sky. Furthermore, the presence of the misalignment calls into question our understanding of the evolution of this binary system.

Unified Astronomy Thesaurus concepts: X-ray sources (1822); Galactic radio sources (571); High mass x-ray binary stars (733); Relativistic jets (1390)

1. Introduction

The archetypal high-mass X-ray binary Cyg X-1, discovered as an X-ray source in 1964 (Bowyer et al. 1965), is probably the best-studied microquasar to date. We have accurate determination of the binary parameters, including the orbital period of $P = 5.599829$ days (Brocksopp et al. 1999), and other parameters (given here as the median values with 68% uncertainties), including the binary inclination, $i = 27\overset{\circ}{.}5^{+0.8}_{-0.6}$; mass of the black hole (BH), $M_{\rm BH} = 21.2 \pm 2.2\ M_\odot$; donor mass, $M_* = 40.6^{+7.7}_{-7.1} M_\odot$; and distance to the source, $D = 2.22^{+0.18}_{-0.17}$ kpc (Miller-Jones et al. 2021, hereafter MJ21). Moreover, the spin parameter of the BH has been measured as $a_* \gtrsim 0.5$ (Kawano et al. 2017) and $\lesssim 1$ (MJ21). This BH spin could not be acquired during accretion given the short lifetime of the system, which implies that it was acquired before the BH formation. Moreover, the low proper motion of Cyg X-1 with respect to its likely parent association Cyg OB3 of $10.7 \pm 2.7\ {\rm km\ s^{-1}}$ (Rao et al. 2020) indicates that the BH was formed with a low natal kick. As then estimated by MJ21, the BH spin axis appears to be inclined by at most 10° from the axis of the binary.

With the launch of the Imaging X-ray Polarimetry Explorer (IXPE; Weisskopf et al. 2022), the issue of a possible misalignment was revived. The polarimetric measurements of Cyg X-1 by IXPE implied that the X-rays are produced in a hot gas that is flattened in the direction orthogonal to the resolved relativistic jet observed in the system (Krawczynski et al. 2022). This configuration corresponds either to the truncated disk geometry (Esin et al. 1997; Poutanen et al. 1997) or to the slab corona geometry (Haardt & Maraschi 1991), whose axis is well aligned in the plane of the sky with the position angle of the jet. The observed high, ≈4%, polarization degree cannot be explained if the inclination of this hot inner region is equal to the orbital inclination; it can be achieved instead if the inclination is higher, $\gtrsim$45°. This discrepancy may indicate a misalignment of the BH spin with respect to the binary axis, implying a geometry where the outer parts of the disk are aligned with the orbital axis and the inner accretion flow is aligned with the BH spin (Bardeen & Petterson 1975).

On the other hand, the position angle of the binary, if assumed equal to the optical polarization angle (Krawczynski et al. 2022), shows good agreement with the X-ray polarization angle and the position angle of the jet. This indicates that the orbital axis and BH spin coincide in the plane of the sky. The misalignment would thus be evident only along the line-of-sight direction.

Since jets are launched along the spin axis of the BH (Blandford & Znajek 1977; McKinney et al. 2013), a BH spin–orbit misalignment should be visible as a jet–orbit one. In the case of jets launched from disks (Blandford & Payne 1982), this will be the case if the inner disk is aligned with the BH spin (Bardeen & Petterson 1975). The arguments above suggest that the jet axis should be inclined at more than 45° with respect to the observer, i.e., misaligned from the orbital plane by $\gtrsim$20°, but in the plane of the sky, the jet direction should coincide with the orbital angular momentum vector. Using the long-term radio light curves of Cyg X-1, we show that this picture is reversed. Namely, we find here compelling evidence for a jet–orbit misalignment in Cyg X-1, which manifests itself on the

Table 1
The Adopted Intervals (in MJD) of the Occurrences of the Hard and Intermediate States

Start	End	Start	End	Start	End	Start	End	Start	End
50,085	50,222	52,853	53,003	55,895	55,940	57,105	57,265	58,631	58,792
50,308	51,845	53,025	53,265	56,035	56,087	57,332	57,970	59,378	59,391
51,858	52,167	53,292	53,368	56,722	56,748	58,112	58,210	59,420	59,860
52,205	52,237	53,385	55,387	56,760	56,845	58,387	58,416		
52,545	52,801	55,674	55,790	57,012	57,045	58,482	58,585		

plane of the sky, while the inclination angles of the binary orbit and the jet coincide within a few degrees.

2. The Data

The radio jet in Cyg X-1 is relatively steady and compact in the hard and hard-intermediate X-ray spectral states (Done et al. 2007) of the source, and is much weaker during the soft states (e.g., Zdziarski et al. 2020), as is typical for accreting BH binaries (Fender et al. 2004).

The radio emission is stable, on average, but shows modulations at the orbital period. A study of the initial 20 month radio light curve of the Ryle Telescope (Jones 1991) revealed strong periodic modulation of emission at 15 GHz (Pooley et al. 1999) with a fractional semiamplitude of ≈0.17. The study found tentative evidence for a lag of the minimum radio flux with respect to the superior conjunction (the phase of the orbit when the compact object is located behind the star) by ≈0.12 of the orbital period and, using the Green Bank Interferometer data at 8.3 and 2.25 GHz, suggested that this lag is increasing with decreasing frequency. A promising interpretation of the lag is the misalignment of the jet axis from that of the binary (Malzac et al. 2009). The quality of the data available at that time, however, did not allow for detailed modeling. By now, the amount of available 15 GHz data from the Ryle Telescope and its successor, the Arcminute Microkelvin Imager Large Array (AMI-LA; Hickish et al. 2018), has increased manyfold. The unprecedentedly long duration of the resulting light curve enables detailed modeling of the orbital modulation, including the accurate determination of the lag.

In our study, we use the radio light curves at 15 GHz from the Ryle Telescope and the AMI-LA (jointly covering MJD 50,226–59,575) and at 8.3 and 2.25 GHz from the Green Bank Interferometer (covering MJD 50,409–51,823) in the hard and hard-intermediate spectral states only. The hard and hard-intermediate state intervals are defined based on the X-ray hardness as in Zdziarski et al. (2020) and given in Table 1. The average fluxes in those states at 15, 8.3, and 2.25 GHz are $\langle F_\nu \rangle = 12.5$, 15.0, and 14.3 mJy, respectively.

We fold and average the light curves over the ephemeris of

$$t_{\rm sup} = t_0 + Pm,\ t_0 = 50077.973,\ P = 5.599829\ \text{days}, \quad (1)$$

where $t_{\rm sup}$ is the time of a superior conjunction (the BH furthest from the observer) in MJD, and m is an integer. This t_0 is below the start times of our light curves, and it fully agrees with the previously given t_0 (Gies et al. 2008).

3. The Model

We use the median values of $M_{\rm BH}$, M_*, D, and i as given in Section 1. The donor radius is $R_* \approx 22\ R_\odot$, and its effective temperature is $T_* \approx 3.1 \times 10^4$ K (MJ21). The masses and orbital period imply a semimajor axis of $a \approx 53\ R_\odot$.

The modulation is due to free–free absorption of the radio emission by the stellar wind from the supergiant donor (Walborn 1973), with the path toward the observer through the wind being orbital phase–dependent. The amplitudes of the modulation can be explained if the radio emission originates in the jet at heights comparable to the stellar separation (Szostek & Zdziarski 2007; Zdziarski 2012). The strongest absorption corresponds to the highest column density of the wind along the path to the observer. For a jet perpendicular to the plane of the sky, this would correspond to the superior conjunction. However, when the jet is significantly inclined, and its approaching part lags behind the binary axis (as projected on the sky), the highest column density occurs at an orbital phase after the superior conjunction. In this Letter, we show that the shapes of the orbital modulation can be well fitted if the jet is misaligned with respect to the binary axis.

We specify the coordinate system and geometry in Figure 1. For simplicity, we assume the orbit to be circular, since the eccentricity is only $\approx 0.019 \pm 0.003$ (MJ21). Movement of the Cyg X-1 binary components in the orbit is clockwise on the sky (MJ21). This implies that the orbital spin vector (along the $+z$-axis) points away from us, and the inclination of that direction is $i_{\rm orb} = 180^\circ - i$, where i is the binary inclination measured using spectroscopic and photometric data (which are not sensitive to the orientation of the orbit). The estimates of its BH spin of $a_* > 0$ imply that rotation of the accretion flow is prograde. Thus, the direction of the BH spin vector and, consequently, the jet spin also points away from the observer and along the counterjet. The standard convention that the superior conjunction corresponds to the orbital phase of $\phi = 0$ requires that the projection of the direction toward the observer onto the binary plane is in the $-x$ direction. The inclination of the BH spin with respect to the binary axis is $\theta_{\rm BH}$, which represents the misalignment of the BH spin vector (and the counterjet) with respect to that of the binary, as well as the misalignment of the jet with respect to the $-z$ direction. The angle of the projection of the BH spin vector onto the binary plane with respect to the $+x$-axis is the azimuthal angle $\phi_{\rm BH}$.

Following the above, the unit vectors pointing toward the observer from the stellar center, to the compact object, and along the jet are

$$\boldsymbol{e}_{\rm obs} = (-\sin i_{\rm orb},\ 0,\ \cos i_{\rm orb}), \quad \boldsymbol{e}_{\rm c} = (\cos\phi,\ \sin\phi,\ 0),$$
$$\boldsymbol{e}_{\rm BH} = (\sin\theta_{\rm BH}\cos\phi_{\rm BH},\ \sin\theta_{\rm BH}\sin\phi_{\rm BH},\ \cos\theta_{\rm BH}), \quad (2)$$

respectively, where $i_{\rm orb} = 180^\circ - i$. Hereafter, we neglect the emission of the counterjet, since Stirling et al. (2001) gave a jet/counterjet ratio of ≈50. We make a simplifying assumption that the modulated emission at a given frequency originates, on average, at a single distance, h, from the BH. We calculate the optical depth starting at the emission point on the jet at the distance h from the BH along the direction toward the observer. The vector connecting the donor center with a point along the

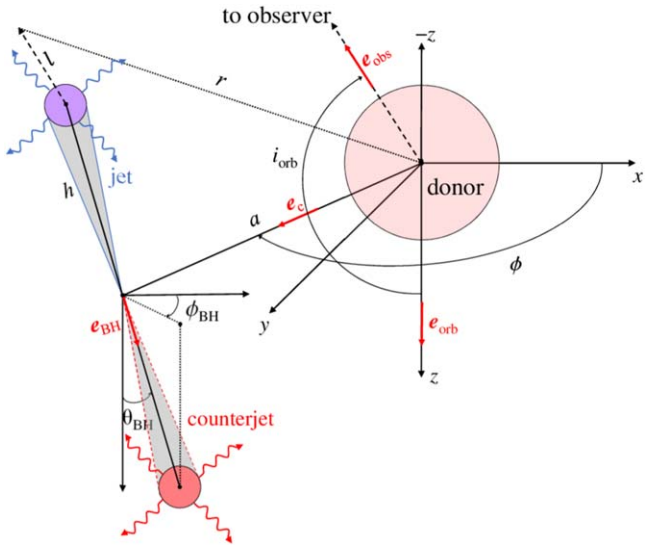

Figure 1. Geometry of the binary and jets. The axes x and y are in the binary plane, and $+z$ gives the direction along the binary vector, $\boldsymbol{e}_{\rm orb}$ (away from the observer, given the observed clockwise rotation). The observer is at an angle, $i_{\rm orb}$, with respect to $\boldsymbol{e}_{\rm orb}$, and ϕ is the orbital phase; $\phi = 0$ and π correspond to the superior and inferior conjunction, respectively. The binary rotation follows the increasing ϕ. The shown configuration is close to the latter. Then, $\theta_{\rm BH}$ is the inclination of the BH spin vector, $\boldsymbol{e}_{\rm BH}$, and the counterjet with respect to $\boldsymbol{e}_{\rm orb}$; $\phi_{\rm BH}$ is its azimuthal angle; and h is the distance of the radio source from the BH center. The counterjet emission is neglected in our model. The distance from the radio source measured along the direction toward the observer is l. The distances of the point at l measured from the centers of the BH and the donor are s (not shown for clarity) and r, respectively.

photon trajectory at the distance l from the emission point is $a\boldsymbol{e}_{\rm c} - h\boldsymbol{e}_{\rm BH} + l\boldsymbol{e}_{\rm obs}$, and the vector connecting the center of the BH with that point at l is $-h\boldsymbol{e}_{\rm BH} + l\boldsymbol{e}_{\rm obs}$. The lengths of these vectors give the distances of that point from the donor and BH centers, and their squares are given by

$$r^2 = (l\cos i_{\rm orb} - h\cos\theta_{\rm BH})^2 + (l\sin i_{\rm orb} - a\cos\phi + h\sin\theta_{\rm BH}\cos\phi_{\rm BH})^2 + (h\sin\theta_{\rm BH}\sin\phi_{\rm BH} - a\sin\phi)^2, \quad (3)$$

$$s^2 = h^2 + l^2 - 2hl\cos i_{\rm orb}\cos\theta_{\rm BH} + 2hl\sin i_{\rm orb}\sin\theta_{\rm BH}\cos\phi_{\rm BH}, \quad (4)$$

respectively. The cosine of the viewing angle of the BH spin vector, $i_{\rm BH}$, is given by $\boldsymbol{e}_{\rm BH}\cdot\boldsymbol{e}_{\rm obs}$, and that of the jet is given by $-\boldsymbol{e}_{\rm BH}\cdot\boldsymbol{e}_{\rm obs}$. The viewing angles of the jet and BH spin are then

$$i_{\rm jet} = \arccos(-\cos i_{\rm orb}\cos\theta_{\rm BH} + \cos\phi_{\rm BH}\sin i_{\rm orb}\sin\theta_{\rm BH}),$$
$$i_{\rm BH} = 180^\circ - i_{\rm jet}, \quad (5)$$

respectively.

We calculate the expected position angle of the projection of the orbital axis on the sky, $\lambda_{\rm orb}$, with respect to the projection of the BH spin, $\lambda_{\rm BH}$. The difference between these two angles (Poutanen et al. 2022) for clockwise rotation on the sky is

$$\Delta\lambda \equiv \lambda_{\rm BH} - \lambda_{\rm orb} = \arccos\frac{\cos\theta_{\rm BH} - \cos i_{\rm BH}\cos i_{\rm orb}}{\sin i_{\rm BH}\sin i_{\rm orb}} = \arccos\frac{\cos i_{\rm orb}\cos\phi_{\rm BH}\sin\theta_{\rm BH} + \sin i_{\rm orb}\cos\theta_{\rm BH}}{\sqrt{1 - (\cos i_{\rm orb}\cos\theta_{\rm BH} - \sin i_{\rm orb}\cos\phi_{\rm BH}\sin\theta_{\rm BH})^2}}, \quad (6)$$

and the observed jet position angle is $\lambda_{\rm jet} = \lambda_{\rm BH} \pm 180^\circ$. Thus, $\lambda_{\rm orb} = \lambda_{\rm jet} - \Delta\lambda \pm 180^\circ$.

Next, we calculate the free–free absorption from a point along the jet at the distance h from the BH center toward the observer, i.e., along the line denoted l in Figure 1. We assume an isotropic stellar wind with the standard velocity profile (Lamers et al. 1987),

$$v(r) \simeq v_\infty\left(1 - \frac{R_*}{r}\right)^\beta, \quad (7)$$

where v_∞ is the terminal wind velocity, and the exponent β determines the acceleration rate. The electron density, n, then follows from the continuity equation at a given mass-loss rate, $\dot{M}$. For simplicity, the presence of ions heavier than hydrogen is neglected. We use $v_\infty = 1.6\times10^8$ cm s^{-1}, $\beta = 1$ (Gies & Bolton 1986), and $\dot{M} = -2.6\times10^{-6}$ yr^{-1} in the hard spectral state (Gies et al. 2003). However, given the likely decrease of the wind density in the polar region (Gies et al. 2008; crossed by the line of sight of the radio photons), we scale that $\dot{M}$ by a factor $f \leqslant 1$.

The free–free absorption coefficient is approximately (Rybicki & Lightman 1979)

$$\alpha_{\rm ff} \approx 0.12\left(\frac{T}{1\ {\rm K}}\right)^{-3/2}\left(\frac{n}{1\ {\rm cm}^{-3}}\right)^2\left(\frac{\nu}{1\ {\rm GHz}}\right)^{-2}{\rm cm}^{-1}. \quad (8)$$

The phase-dependent optical depth to free–free absorption is

$$\tau(\phi) = \tau_0\left(\frac{\nu}{15\ {\rm GHz}}\right)^{-2} \times\int_0^\infty\left[\frac{r(l)}{a}\right]^{-4}\left[1 - \frac{R_*}{r(l)}\right]^{-2\beta}\left\{\frac{T[r(l),\, s(l)]}{T_0}\right\}^{-3/2}\frac{{\rm d}l}{a}, \quad (9)$$

where τ_0 is a reference optical depth defined at 15 GHz, the density at $r = a$ under the assumption of $v = v_\infty$, the distance a, and at a reference temperature, T_0,

$$\tau_0 \approx 26.3\left(\frac{-f\dot{M}}{2.6\times10^{-6}\,M_\odot\ {\rm yr}^{-1}}\right)^2\left(\frac{M_* + M_{\rm BH}}{62M_\odot}\right)^{-1} \times\left(\frac{v_\infty}{1.6\times10^8\ {\rm cm\ s}^{-1}}\right)^{-2}\left(\frac{T_0}{10^6\ {\rm K}}\right)^{-3/2}. \quad (10)$$

The observed flux is

$$F(\phi) = F_{\rm intr}\exp[-\tau(\phi)], \quad (11)$$

where $F_{\rm intr}$ is the flux before the absorption. We calculate $\tau(\phi)$ numerically using $T(r, s)$ from the solution of the energy balance equation including Compton and photoionization heating and Compton recombination and line cooling (Zdziarski 2012). The ionizing X-ray luminosity is estimated as $L_{\rm ion} \approx 2\times10^{37}$ erg s^{-1}. The radiative heating and cooling of the wind at distance l from the emission point is by both the emission of the donor and the X-rays. However, we do not include the adiabatic cooling. Such cooling would lead to a strong temperature decrease (Zdziarski 2012) at $r \gtrsim a$ and the associated strong increase of the absorption coefficient. Our neglect of that cooling is motivated by the wind expansion being, to a good approximation, in vacuum, with the wind density at the radii of interest (e.g., $n \sim 10^{10}$ cm^{-3} at $r = a$) being orders of magnitude higher than the density of the interstellar medium, which is also swept away by

Table 2
Fit Results Based on the MCMC Method

b	h_{15}/a	f	i (deg)	$\theta_{\rm BH}$ (deg)	$\phi_{\rm BH}$ (deg)	$\frac{\langle F_{\rm intr,15}\rangle}{\langle F_{15}\rangle}$	$\frac{h_8}{h_{15}}$	$\frac{\langle F_{\rm intr,8}\rangle}{\langle F_8\rangle}$	$\frac{h_2}{h_{15}}$	$\frac{\langle F_{\rm intr,2}\rangle}{\langle F_2\rangle}$	$\frac{\chi^2}{\rm d.o.f.}$	$i_{\rm jet}$ (deg)	$\Delta\lambda$ (deg)
0f	$2.9^{+1.4}_{-1.8}$	$0.8^{+0.2}_{-0.5}$	27.5f	23^{+13}_{-8}	76^{+16}_{-8}	$1.24^{+0.11}_{-0.06}$	$1.7^{+0.5}_{-0.2}$	$1.15^{+0.09}_{-0.07}$	$9.3^{+9.5}_{-5.2}$	$1.02^{+0.12}_{-0.02}$	36/35	31^{+6}_{-2}	47^{+24}_{-17}
0.5f	$2.4^{+1.1}_{-1.5}$	$0.8^{+0.2}_{-0.4}$	27.5f	22^{+11}_{-6}	76^{+16}_{-8}	$1.49^{+0.15}_{-0.12}$	$1.7^{+0.6}_{-0.2}$	$1.29^{+0.17}_{-0.14}$	$9.1^{+9.6}_{-5.0}$	$1.03^{+0.21}_{-0.03}$	37/35	31^{+4}_{-3}	46^{+20}_{-14}

Note. The table gives the median values and their 90% confidence ranges, while the χ^2 values are given for the best fits. Fixed parameters are marked by "*f*." The jet viewing angle, $i_{\rm jet}$, and the differences in the position angles on the sky, $\Delta\lambda$, are derived quantities rather than free parameters. The $b = 0.5$ case (marked in bold) represents our final results, for which the values of $\langle F_{{\rm intr},\nu}\rangle/\langle F_\nu\rangle$ refer to the modulated component only.

the wind. Thus, the wind does not perform *pdV* work on the surrounding medium. The expansion can lead the particle distribution to be anisotropic and different from a Maxwellian, whose minor effect we neglect.

We then consider the spatial distribution of the radio emission along the jet. Resolved radio maps (Stirling et al. 2001; Rushton et al. 2010) imply that a fraction of ≈0.3–0.5 of the 8 GHz emission is emitted at distances $\gtrsim 2\times10^{14}$ cm, which is $\gtrsim 50a$. A similar constraint follows from the measured long radio lag with respect to X-rays (Tetarenko et al. 2019). However, if most of the radio flux originated from such distances, orbital modulation would have been negligible.

On the other hand, we can calculate the photospheric distance from jet models. The hard-state 2–220 GHz spectrum of Cyg X-1 (Fender et al. 2000) is approximately flat with $\alpha\approx 0$ (where the flux density $F_\nu\propto\nu^\alpha$). The simplest and widely adopted model of such a spectrum is partially self-absorbed synchrotron emission with the distributions of both nonthermal electrons and the magnetic energy flux maintained along the jet (Blandford & Königl 1979). The location of the bulk of the emission at a given frequency in this model approximately corresponds to the unit optical depth to synchrotron self-absorption. For that, we use a previous formulation (Zdziarski et al. 2022). For the parameters of Cyg X-1, that distance is given by

$$\frac{h_\nu}{a}\approx 2.8\frac{15{\rm GHz}}{\nu}\left(\frac{\sin 27.^\circ 5}{\sin i_{\rm jet}}\right)^{\frac{5+p}{13+2p}}\left(\frac{\langle F_\nu\rangle}{10{\rm mJy}}\right)^{\frac{6+p}{13+2p}}\left(\frac{1^\circ}{\Theta}\right)^{\frac{7+p}{13+2p}}, \tag{12}$$

where $2.8a\approx 1.0\times10^{13}$ cm; Θ is the jet opening angle, which has been estimated as ≈0.°4–1.°8 (Tetarenko et al. 2019); and p is the steady-state power-law index of the relativistic electrons, which is consistent with ≈2.5–3.5 (Zdziarski et al. 2014). The dependencies of h_ν on the ratio of the gas-to-magnetic energy densities and the minimum and maximum energies of the relativistic electrons are very weak. The range of values implied by Equation (12), $h_\nu\approx(1.6\text{–}5.4)a$, is $\ll 50a$ and consistent with the observed strong orbital modulations.

The above considerations imply a relatively complex radio emission profile, which we approximate as two separate regions of the radio emission. Namely, we split the folded and averaged radio light curves, $F_\nu(\phi)$, into the modulated, $F_\nu^{\rm mod}$, and unmodulated parts,

$$F_\nu(\phi)=F_\nu^{\rm mod}(\phi)+b\langle F_\nu\rangle,\quad \Delta F_\nu^{\rm mod}(\phi)=\Delta F_\nu(\phi),$$
$$\frac{\Delta F_\nu^{\rm mod}(\phi)}{F_\nu^{\rm mod}(\phi)}\approx\frac{\Delta F_\nu(\phi)}{(1-b)F_\nu(\phi)}, \tag{13}$$

where $\Delta F_\nu(\phi)$ is the uncertainty of $F_\nu(\phi)$, and b is the unmodulated fraction. We use $b = 0.5$ as a likely value. The unmodulated part accounts for the remote emission. However, we also perform the calculations at $b = 0$. We find that the two sets of fitted parameters are very similar (see Table 2), which shows that our results are not sensitive to the assumed value of b.

4. Results

We fit our model to the three folded light curves simultaneously. In order to estimate the uncertainties of the fit, we use both the method based on $\Delta\chi^2$, where χ^2 is the fit statistics (Lampton et al. 1976), and the Markov Chain Monte Carlo (MCMC) method (Sanders 2012; Foreman-Mackey et al. 2013), both as implemented in XSPEC (Arnaud 1996). In the latter, we assume wide normal priors centered on the best-fit parameters with the widths estimated from the linear error estimates. Both methods give very similar results, and we present only those based on the MCMC. The fit results are given in Table 2, and the folded light curves are shown in Figure 2. Figure 3 shows the parameter distributions and correlations for the case of $b = 0.5$. The statistical quality of the fits is very good, with the reduced $\chi^2\approx 1$. Table 2 shows that the main difference between the results obtained for $b = 0$ and 0.5 is the larger ratios of the intrinsic to the observed fluxes for the modulated component at $b = 0.5$. We find a significant BH spin–orbit misalignment of 16°–33° and an azimuthal angle of 68°–92°. These two angles account for the lags seen in the orbital modulations. The emission heights are determined primarily by the modulation amplitudes, and the misalignment angle results jointly from the lags and the heights. The azimuthal angle is close to 90°; i.e., the jet is bent close to the plane of the sky. The attenuation is very modest at each frequency, compatible with the average radio spectrum being approximately a single power law (Fender et al. 2000).

The presence of a misalignment has a very high statistical significance. When we fix the misalignment angle $\Theta_{\rm BH} = 0$ (as well as $\phi_{\rm BH}$ at any value, which then has no influence on the fit), we obtain a very high value of χ^2/d.o.f. of 402/37 compared to 37/35 for the model with a misalignment. The F-test probability of the fit improvement being by chance (Lampton et al. 1976) when allowing for a misalignment is $\approx 7\times10^{-19}$. With this model, we also measure the phase lags, i.e., the phases of the minima of the phase-folded fluxes. We keep the assumption of $\Theta_{\rm BH} = 0$ but introduce phenomenological phase lags, $\Delta\phi$, with respect to the superior conjunction to the light curves. The obtained values are given in Table 3 for $b = 0$ and 0.5; the values are almost identical for the two. The hypothesis of no lags has the same statistical significance as that of the lack of a misalignment.

Table 2 gives the jet viewing angle, $i_{\rm jet}$ (Equation (5)). We see that, due to the fitted relative jet orientation with respect to the binary axis and the observer, it is similar to the binary

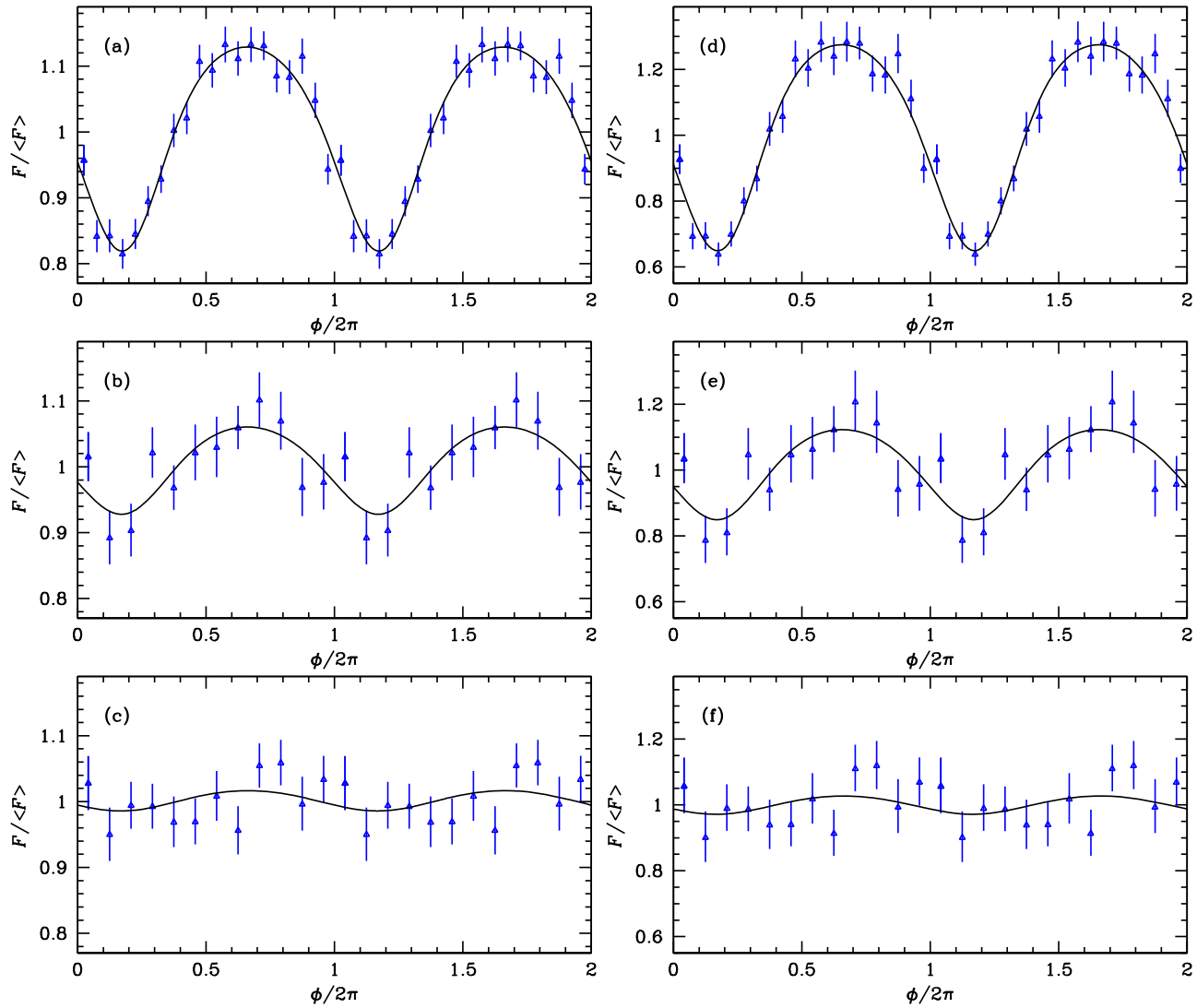

Figure 2. Observed orbital modulations fitted by our model (solid curves). The left and right panels assume that 100% ($b = 0$) and 50% ($b = 0.5$) of the total flux is modulated, respectively. (a) 15 GHz, (b) 8.3 GHz, (c) 2.25 GHz, (d) 15 GHz, (e) 8.3 GHz, (f) 2.25 GHz. For clarity, two cycles are shown.

inclination, i. On the other hand, we find a relatively large difference between the BH position angle on the sky, $\lambda_{\rm BH}$ (equal to that of the jet $\pm 180°$; Equation (6)), and the implied position angle, $\lambda_{\rm orb}$, of the binary axis, $\Delta\lambda \approx 32°$–$66°$. The values of $i_{\rm jet}$ and $\Delta\lambda$ depend on all of $i_{\rm orb}$, $\Theta_{\rm BH}$, and $\phi_{\rm BH}$.

Figure 4 shows the image of the jet in Cyg X-1 from a 1998 VLBA/VLA observation (Stirling et al. 2001). The position angle of the inner part of the jet is $\lambda_{\rm jet} \approx -17°$ (we note that it changed to $-26°$ in the 2016 observations; MJ21). We show here the orbital position angle, $\lambda_{\rm orb}$. Due to the obtained large $\Delta\lambda$ (Table 2), $\lambda_{\rm orb} \approx 88°$–$131°$ is very different from the jet position angle.

5. Discussion

Our model fits the data very well and gives the parameters in full agreement with the standard jet model (Blandford & Königl 1979). The fitted height of the 15 GHz emission of $2.4^{+1.1}_{-1.5}a$ fully agrees with the estimate of Equation (12), as well as with more detailed calculations (Zdziarski et al. 2014). Then, the fitted location of the 8.3 GHz emission agrees (and that of 2.25 GHz is consistent) with the standard scaling (Blandford & Königl 1979) of $h \propto \nu^{-1}$.

The misalignment of the BH spin axis with respect to the binary one implies that the spin axis will precess. We use a post-Newtonian estimate (Barker & O'Connell 1975; Apostolatos et al. 1994), which, together with the Kepler law, gives a de Sitter precession period of

$$P_{\rm prec} = \frac{c^2 (M_* + M_{\rm BH})^{4/3} P^{5/3}}{(2\pi G)^{2/3} (2 + 3M_*/2M_{\rm BH}) M_* M_{\rm BH}}, \qquad (14)$$

where G is the gravitational constant. For the best-fit parameters of Cyg X-1, $P_{\rm prec} \approx 5.6$ kyr. While this is a negligible effect for observations of the jet, it has important implications for the origin of the interstellar shell apparently powered by the jet (Gallo et al. 2005). In that scenario, the jet lifetime is estimated to be between 17 and 63 kyr (Russell et al. 2007), i.e., from a few to $\sim 10 P_{\rm prec}$. Given our calculated misalignment angle, the jet would affect a larger structure than that observed. However, the origin of that structure from the jet of Cyg X-1 appears uncertain. No analogous structure due to

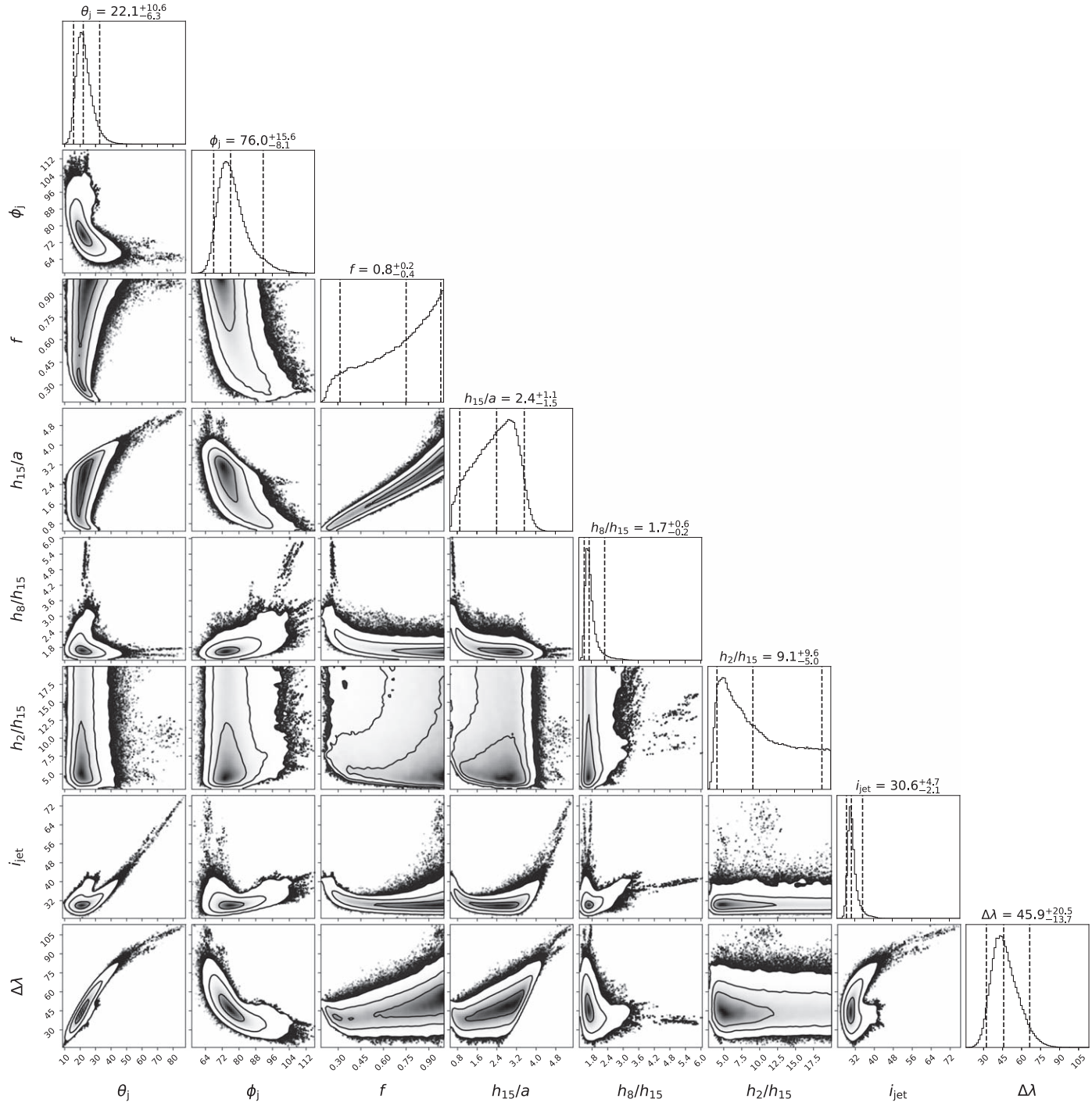

Figure 3. The MCMC results for the case of $b = 0.5$. The panels show the histograms of the one-dimensional posterior distributions for the model parameters and the two-parameter correlations. The median results for the fitted quantities are shown by the middle vertical dashed lines in the distribution panels. The surrounding vertical dashed lines correspond to the 90% uncertainty. The parameters obtained are given above the posterior distributions.

Table 3
Estimated Phase Lags

b	$\Delta\phi_{15}/2\pi$	$\Delta\phi_8/2\pi$	$\Delta\phi_2/2\pi$
0f	$0.17^{+0.01}_{-0.01}$	$0.17^{+0.06}_{-0.07}$	$0.35^{+0.13}_{-0.15}$
0.5f	$0.17^{+0.01}_{-0.01}$	$0.17^{+0.06}_{-0.07}$	$0.35^{+0.14}_{-0.16}$

Note. These lags are measured with respect to the model with $\Theta_{BH} = 0$ and $\Delta\phi$ added as a phenomenological parameter. Thus, they can differ slightly from the positions of the peaks of the model orbital modulation in Figure 2.

the counterjet has been confirmed (Russell et al. 2007), and there is still no definite model of the shell (Sell et al. 2015).

We find that the jet viewing angle, i_{jet}, is similar to the binary inclination, i. This finding does not support the interpretation of the system misalignment along the line of sight, which was put forward as an explanation of the high X-ray polarization (Krawczynski et al. 2022). Our results imply that if the inner flow is perpendicular to the BH spin (Bardeen & Petterson 1975), the inclination of that flow is similar to that of the binary, in spite of the jet misalignment. Thus, the strong

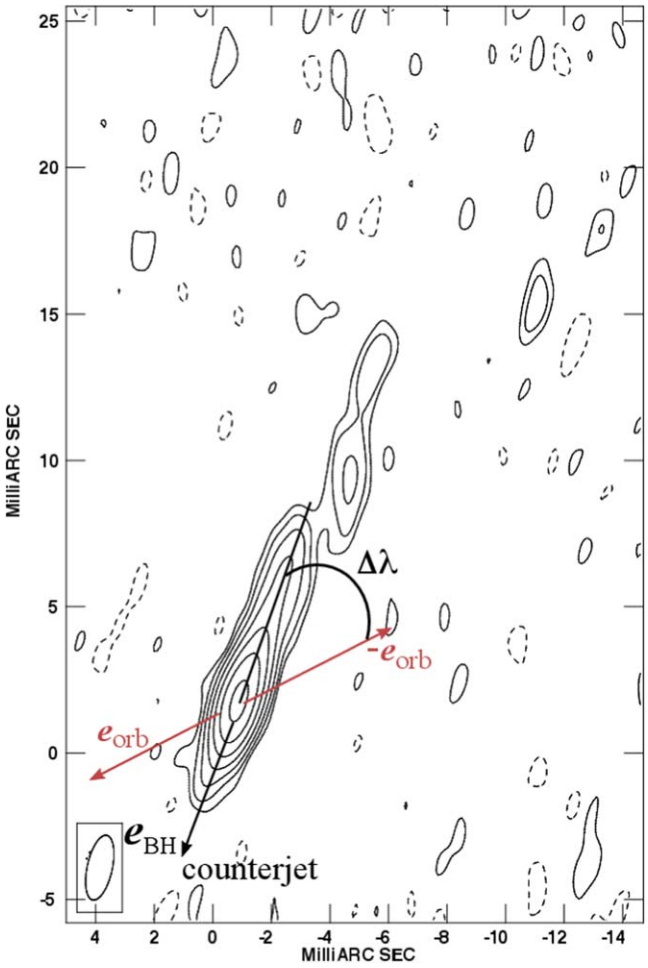

Figure 4. Image of the jet obtained with the VLBA/VLA observation (Stirling et al. 2001) on 1998 August 10 at 8.4 GHz. We show the projected position vectors of the orbit and the spin of the BH.

X-ray polarization has to have another origin, likely coronal outflows (Poutanen et al. 2023).

Furthermore, our modeling implies that the jet should be inclined with respect to the binary axis in the plane of the sky; the angle between these two axes is $\Delta\lambda \approx 32°$–$66°$. This conclusion is surprising in light of the earlier suggestion that the orbital axis, as probed by the position angle of the optical polarization, is well aligned with the position angle of the X-ray polarization and the axis of the radio jet (Krawczynski et al. 2022; Kravtsov et al. 2023). Our findings suggest that the optical polarization should not be related to the binary axis, as previously thought (Kemp et al. 1978, 1979). Instead, it may arise from scattering in a cocoon surrounding the jet, formed by the jet's interaction with the wind of the companion star or the interstellar medium (Bicknell et al. 1997). In this case, the mean polarization angle would be aligned with the jet. Further thorough analysis of the optical polarization data is needed to verify this suggestion. On the other hand, we have checked that our implied astrometric solution (with the jet misalignment) is approximately consistent with the radio orbital displacements (MJ21).

The presence of the binary/BH misalignment is in conflict with our current evolutionary scenario for Cyg X-1 (MJ21). One possible explanation for this discrepancy is that Cyg X-1 is not a member of the Cyg OB3 association. While the current determinations of their distances, $2.22^{+0.18}_{-0.17}$ and 1.92 ± 0.31 kpc (Rao et al. 2020), respectively, are compatible with each other, Cyg X-1 could still not be a member. Projected on the sky, Cyg X-1 is on the edge of the OB3 association and was considered a field star in a previous clustering analysis (Mel'Nik & Efremov 1995). Alternatively, Cyg X-1 may still be a member of the OB3 association, but the maximum asymmetric natal kick could be higher than the assumed (MJ21) 10–20 km s^{-1}. In fact, a recent study (Tauris 2022) has shown that the observed distribution of inspiral spins of merging BHs, showing a strong tail of negative values, is in clear tension with the current theoretical models of binary evolution and supernovae. Tauris (2022) showed that the discrepancy can be resolved if some BHs have their spins tossed in a random direction during their formation and proposed some tentative mechanisms for the tossing. The misalignment in Cyg X-1 could be due to such a process.

We then consider alternative interpretations of the phase lags. First, the wind accretion in Cyg X-1 is focused toward the BH with the donor almost filling the Roche lobe (MJ21). The wind crossing the L1 point could then be asymmetric, but the maximal absorption is expected at phases before the superior conjunction (due to the Coriolis force; Frank et al. 1987), contrary to what we see. Furthermore, the X-rays from the system, which originate close to the BH, are orbitally modulated as well due to bound–free absorption and Compton scattering by the same wind. Their flux minima are observed without any measurable lag (Pooley et al. 1999; Wen et al. 1999; Lachowicz et al. 2006) with respect to the spectroscopically determined superior conjunction, which shows that any effects of the wind asymmetry on the absorption are negligible. The impact of the wind on the jet can also bend it in the direction along the wind (Bosch-Ramon & Barkov 2016), i.e., with the jet bent outside and precessing at the binary period, which is neither observed in Cyg X-1 nor would lead to the absorption lags.

Second, the jet trajectory could be helical due to the circular motion of the BH with respect to the center of mass of the binary (Szostek & Zdziarski 2007; Bosch-Ramon & Barkov 2016). This could explain the observed radio phase lags, but only if the jet velocity within a distance of $\lesssim 30a$ were nonrelativistic (Szostek & Zdziarski 2007). This disagrees with the jet velocity close to the speed of light inferred from the apparent absence of an observed counterjet (according to Stirling et al. 2001) and the lag of the radio emission with respect to the X-rays (Tetarenko et al. 2019). However, this might still be possible if the jet consists of a slow and nonradiating sheath collimating a fast and radiating spine (Ferreira et al. 2006), as has been proposed (Szostek & Zdziarski 2007).

Our finding of the jet–orbit misalignment in Cyg X-1 makes it a member of a small group of X-ray binaries with unambiguous observational evidence for misalignments. The others are GRO J1655–40 (Hjellming & Rupen 1995; Beer & Podsiadlowski 2002), Cyg X-3 (Zdziarski et al. 2018), and MAXI J1820+070 (Poutanen et al. 2022).

6. Conclusions

Using an unprecedentedly long light curve of Cyg X-1 at 15 GHz, together with light curves at 8.3 and 2.25 GHz radio frequencies, we obtain strong evidence for a misalignment of its jet with respect to the orbital axis. The misalignment is

inferred from the presence of significant delays of the minima of the radio light curves with respect to the times of superior conjunction. The observed strong orbital modulation of the radio flux is due to absorption of the jet emission by the stellar wind of the donor, which depends on the orbital phase. If the jet were aligned with the orbital axis, the maximal absorption—and the minimum of the radio flux—would be expected at the phase of the superior conjunction. The observed delays instead unambiguously show that the sources of the radio emission are displaced from the symmetry plane of the binary (defined by the semimajor axis and the normal to the binary plane). Thus, the jet at the location of the radio emission jet is inclined with respect to the binary axis; we find the misalignment angle to be $\approx 16°$–$33°$.

However, we find that the jet inclination is approximately the same as the binary inclination, in contrast to the earlier suggestion of a misalignment lying predominantly along the line of sight, motivated by the X-ray polarization studies. Moreover, we find that the projection on the sky of the orbital axis is clearly different from that of the radio jet. This finding has implications for the production of the optical polarization. Finally, the presence of the misalignment in Cyg X-1 disagrees at face value with the evolutionary arguments. It implies that either Cyg X-1 is not a member of the Cyg OB3 association or the kick it received during the BH formation was higher than previously estimated.

Acknowledgments

We thank Richard O'Shaughnessy for a consultation, Rob Fender for permission to use Figure 3 of Stirling et al. (2001) in our Figure 4, and James Miller-Jones and Arash Bahramian for advice with using their astrometry script. We also thank the referees for valuable comments. We acknowledge the staff who operate and run the AMI-LA telescope at the Mullard Radio Astronomy Observatory, Lord's Bridge, Cambridge. AMI is supported by the European Research Council under grant ERC-2012-StG-307215 LODESTONE. A.A.Z. and M.S. acknowledge support from the Polish National Science Center under grants 2019/35/B/ST9/03944 and 2017/27/B/ST9/01940, and the University of Łódź IDUB grant, decision No. 59/2021, respectively. Nordita is supported in part by NordForsk. This research was supported by the International Space Science Institute (ISSI) in Bern, through ISSI International Team project #486.

ORCID iDs

Andrzej A. Zdziarski https://orcid.org/0000-0002-0333-2452
Alexandra Veledina https://orcid.org/0000-0002-5767-7253
Michał Szanecki https://orcid.org/0000-0001-7606-5925
David A. Green https://orcid.org/0000-0003-3189-9998
Joe S. Bright https://orcid.org/0000-0002-7735-5796
David R. A. Williams https://orcid.org/0000-0001-7361-0246

References

Apostolatos, T. A., Cutler, C., Sussman, G. J., & Thorne, K. S. 1994, PhRvD, 49, 6274
Arnaud, K. A. 1996, in ASP Conf. Ser. 101, XSPEC: The First Ten Years, ed. G. H. Jacoby & J. Barnes (San Francisco, CA: ASP), 17
Bardeen, J. M., & Petterson, J. A. 1975, ApJL, 195, L65
Barker, B. M., & O'Connell, R. F. 1975, PhRvD, 12, 329
Beer, M. E., & Podsiadlowski, P. 2002, MNRAS, 331, 351
Bicknell, G. V., Dopita, M. A., & O'Dea, C. P. O. 1997, ApJ, 485, 112
Blandford, R. D., & Königl, A. 1979, ApJ, 232, 34
Blandford, R. D., & Payne, D. G. 1982, MNRAS, 199, 883
Blandford, R. D., & Znajek, R. L. 1977, MNRAS, 179, 433
Bosch-Ramon, V., & Barkov, M. V. 2016, A&A, 590, A119
Bowyer, S., Byram, E. T., Chubb, T. A., & Friedman, H. 1965, Sci, 147, 394
Brocksopp, C., Tarasov, A. E., Lyuty, V. M., & Roche, P. 1999, A&A, 343, 861
Done, C., Gierliński, M., & Kubota, A. 2007, A&ARv, 15, 1
Esin, A. A., McClintock, J. E., & Narayan, R. 1997, ApJ, 489, 865
Fender, R. P., Belloni, T. M., & Gallo, E. 2004, MNRAS, 355, 1105
Fender, R. P., Pooley, G. G., Durouchoux, P., Tilanus, R. P. J., & Brocksopp, C. 2000, MNRAS, 312, 853
Ferreira, J., Petrucci, P. O., Henri, G., Saugé, L., & Pelletier, G. 2006, A&A, 447, 813
Foreman-Mackey, D., Hogg, D. W., Lang, D., & Goodman, J. 2013, PASP, 125, 306
Frank, J., King, A. R., & Lasota, J. P. 1987, A&A, 178, 137
Gallo, E., Fender, R., Kaiser, C., et al. 2005, Natur, 436, 819
Gies, D. R., & Bolton, C. T. 1986, ApJ, 304, 389
Gies, D. R., Bolton, C. T., Blake, R. M., et al. 2008, ApJ, 678, 1237
Gies, D. R., Bolton, C. T., Thomson, J. R., et al. 2003, ApJ, 583, 424
Haardt, F., & Maraschi, L. 1991, ApJL, 380, L51
Hickish, J., Razavi-Ghods, N., Perrott, Y. C., et al. 2018, MNRAS, 475, 5677
Hjellming, R. M., & Rupen, M. P. 1995, Natur, 375, 464
Jones, M. E. 1991, in ASP Conf. Ser. 19, IAU Colloq. 131: Radio Interferometry. Theory, Techniques, and Applications, ed. T. J. Cornwell & R. A. Perley (San Francisco, CA: ASP), 395
Kawano, T., Done, C., Yamada, S., et al. 2017, PASJ, 69, 36
Kemp, J. C., Barbour, M. S., Herman, L. C., & Rudy, R. J. 1978, ApJL, 220, L123
Kemp, J. C., Barbour, M. S., Parker, T. E., & Herman, L. C. 1979, ApJL, 228, L23
Kravtsov, V., Veledina, A., Berdyugin, A. V., et al. 2023, A&A, in press (arXiv:2305.10813)
Krawczynski, H., Muleri, F., Dovčiak, M., et al. 2022, Sci, 378, 650
Lachowicz, P., Zdziarski, A. A., Schwarzenberg-Czerny, A., Pooley, G. G., & Kitamoto, S. 2006, MNRAS, 368, 1025
Lamers, H. J. G. L. M., Cerruti-Sola, M., & Perinotto, M. 1987, ApJ, 314, 726
Lampton, M., Margon, B., & Bowyer, S. 1976, ApJ, 208, 177
Malzac, J., Belmont, R., & Fabian, A. C. 2009, MNRAS, 400, 1512
McKinney, J. C., Tchekhovskoy, A., & Blandford, R. D. 2013, Sci, 339, 49
Mel'Nik, A. M., & Efremov, Y. N. 1995, AstL, 21, 10
Miller-Jones, J. C. A., Bahramian, A., Orosz, J. A., et al. 2021, Sci, 371, 1046
Pooley, G. G., Fender, R. P., & Brocksopp, C. 1999, MNRAS, 302, L1
Poutanen, J., Krolik, J. H., & Ryde, F. 1997, MNRAS, 292, L21
Poutanen, J., Veledina, A., & Beloborodov, A. M. 2023, ApJL, 949, L10
Poutanen, J., Veledina, A., Berdyugin, A. V., et al. 2022, Sci, 375, 874
Rao, A., Gandhi, P., Knigge, C., et al. 2020, MNRAS, 495, 1491
Rushton, A., Miller-Jones, J. C. A., Paragi, Z., et al. 2010, PoS, 10, 61
Russell, D. M., Fender, R. P., Gallo, E., & Kaiser, C. R. 2007, MNRAS, 376, 1341
Rybicki, G. B., & Lightman, A. P. 1979, Radiative Processes in Astrophysics (New York: Wiley)
Sanders, J. 2012, xspec_emcee, GitHub, https://github.com/jeremysanders/xspec_emcee
Sell, P. H., Heinz, S., Richards, E., et al. 2015, MNRAS, 446, 3579
Stirling, A. M., Spencer, R. E., de la Force, C. J., et al. 2001, MNRAS, 327, 1273
Szostek, A., & Zdziarski, A. A. 2007, MNRAS, 375, 793
Tauris, T. M. 2022, ApJ, 938, 66
Tetarenko, A. J., Casella, P., Miller-Jones, J. C. A., et al. 2019, MNRAS, 484, 2987
Walborn, N. R. 1973, ApJL, 179, L123
Weisskopf, M. C., Soffitta, P., Baldini, L., et al. 2022, JATIS, 8, 026002
Wen, L., Cui, W., Levine, A. M., & Bradt, H. V. 1999, ApJ, 525, 968
Zdziarski, A. A. 2012, MNRAS, 422, 1750
Zdziarski, A. A., Malyshev, D., Dubus, G., et al. 2018, MNRAS, 479, 4399
Zdziarski, A. A., Pjanka, P., Sikora, M., & Stawarz, Ł. 2014, MNRAS, 442, 3243
Zdziarski, A. A., Shapopi, J. N. S., & Pooley, G. G. 2020, ApJL, 894, L18
Zdziarski, A. A., Tetarenko, A. J., & Sikora, M. 2022, ApJ, 925, 189